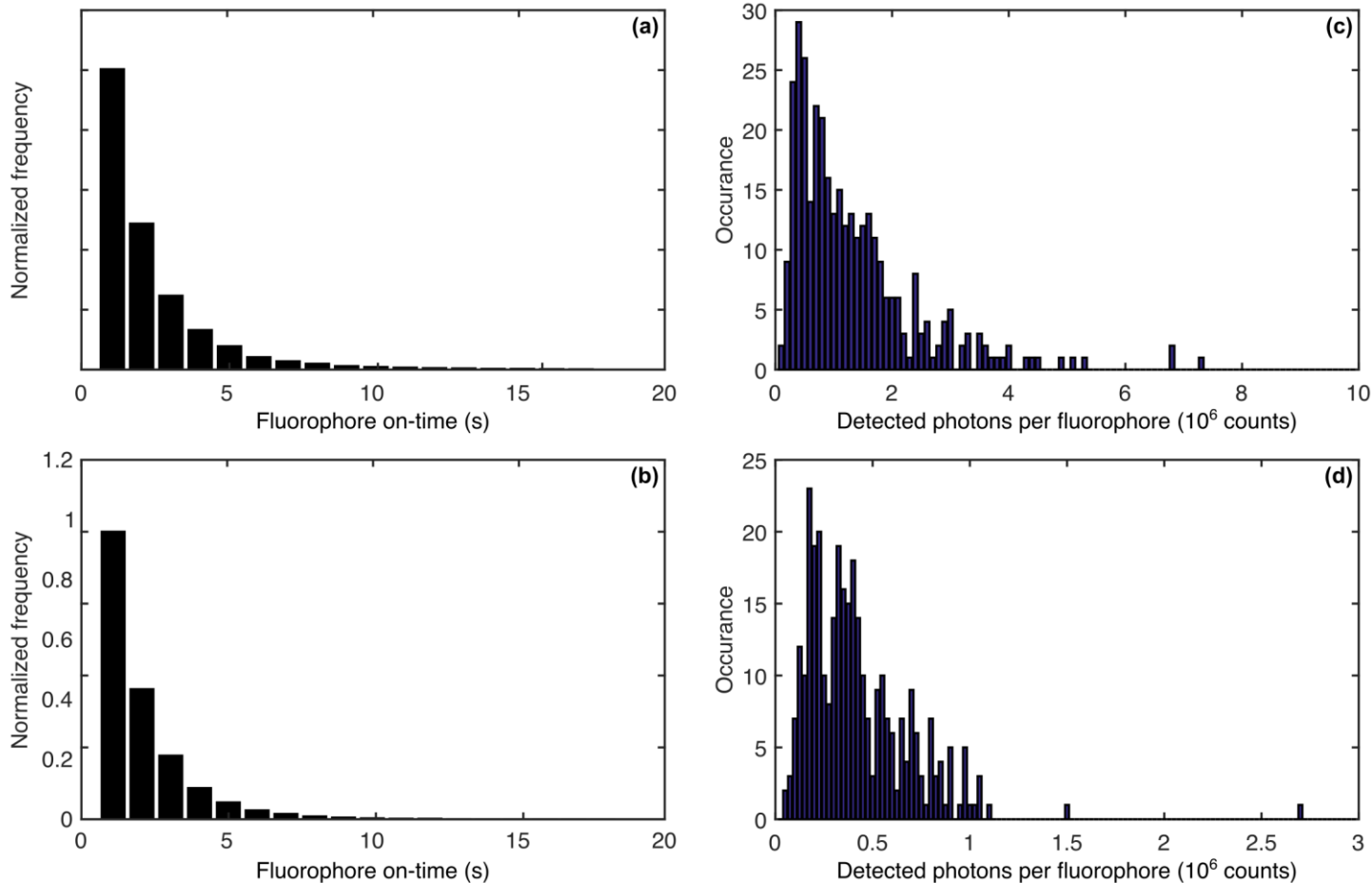**Supplementary Figure 1**

**Control experiments on the fluorescence stability of single Atto647N-biotin complexes.**

a, Exemplary signal trace (black line) in counts per second (cps) of a single Atto647N molecule attached to a single biotin molecule with linear combination fit (N = 1, red dots). **b**, Plot of the difference between the fit and the experimental trace, yielding RMS = 37 cps. The fit error is 2.9 times the shot noise. The integration time per point was chosen to be 2 seconds as an empirical compromise to minimize fluctuations due to fast blinking events (as in our other measurements in the manuscript). **c,** Histogram of the shot-noise-corrected fit error for many single Atto647n-biotin molecules.

Supplementary Figure 2

Fluorophore on-times and photon numbers.

On-time photoblinking statistics at liquid helium temperature for individual Atto647N molecules coupled to PASc (**a**) and coupled to streptavidin via biotin (**b**). Histograms of the detected number of photons per fluorophore for the PASc domain dimer (**c**) and the streptavidin molecule (**d**). The histograms show the detected number of photons per fluorophore on a protein complex. Since in the case of streptavidin there are possible intensity combinations, each molecule is less often observed alone. This reduces the average total number of detected photons per fluorophore during the same observation time.
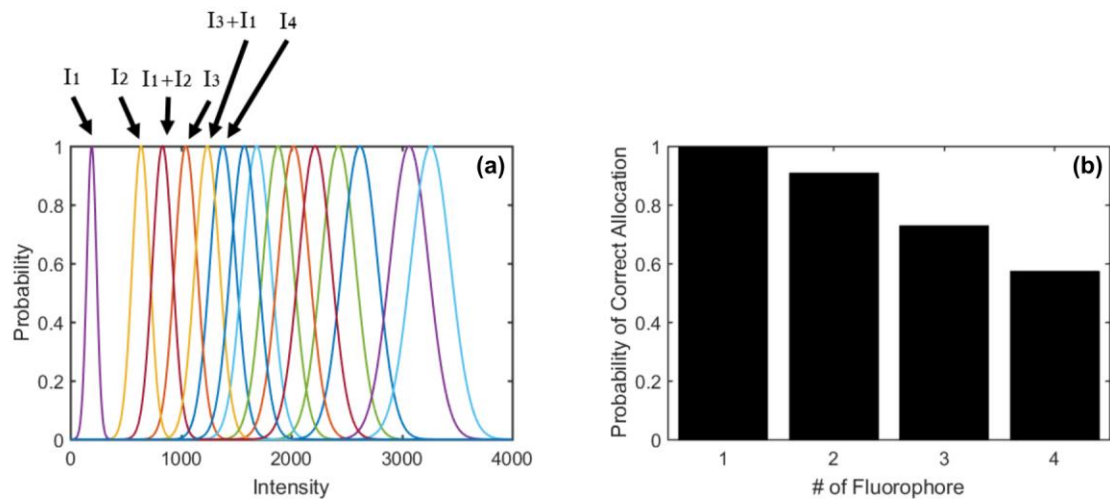
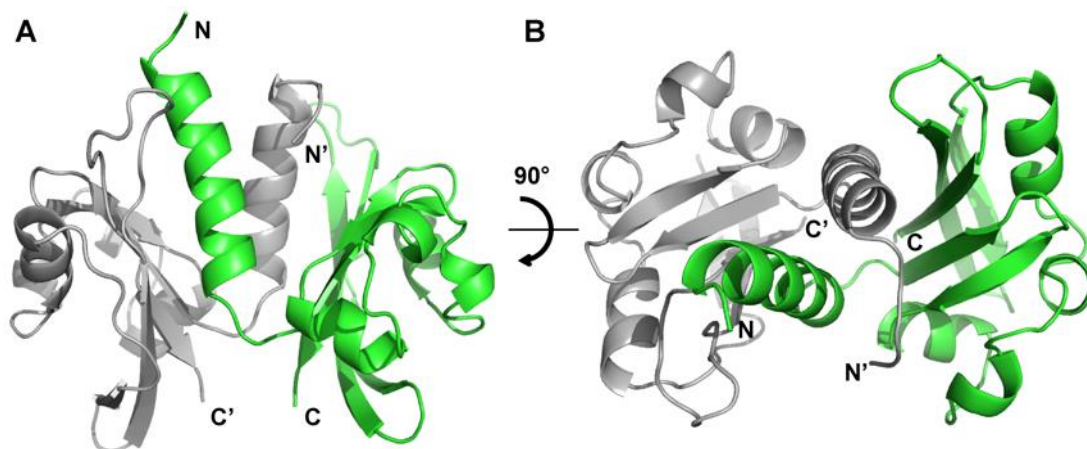**Supplementary Figure 3**

Intensity level allocation.

a, Visualization of the uncertainty in determining the position of each intensity level for an example streptavidin recording. Normal distributions (various colors) are plotted at the determined positions with their widths encoding the experimentally observed fit error. The variables of the fitting procedure (intensity levels of the individual fluorophores $I_1..I_4$) are marked as well as some linear combination levels. **b,** Probability of the correct allocation of a measured intensity to the estimated intensity level as a function of the number of fluorophores.
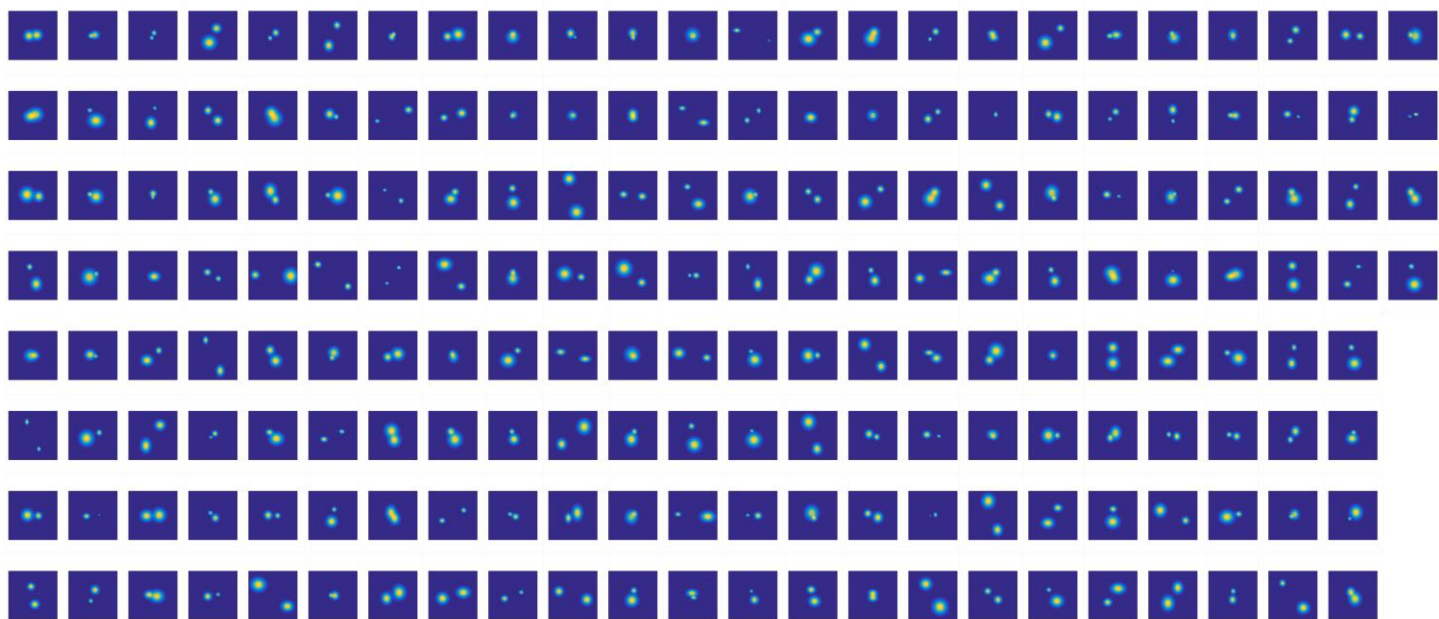
Supplementary Figure 4

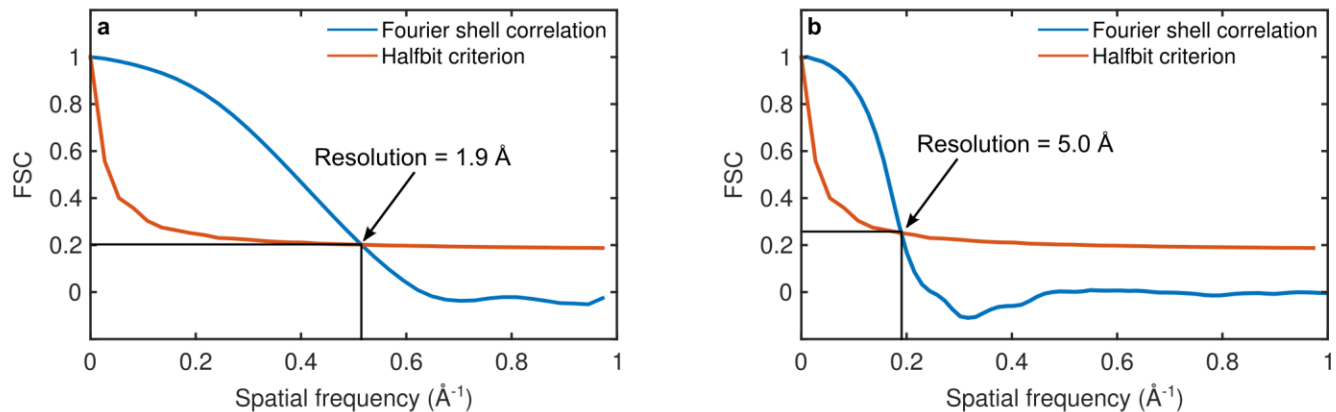**Complete data sets from the PASc domain dimer measurements.**

Data for localization precisions better than 6.5 Å. Black crosses indicate the measured positions while the precision is encoded as the width of the 2D Gaussian probability distributions. Plots are 5 x 5 nm.

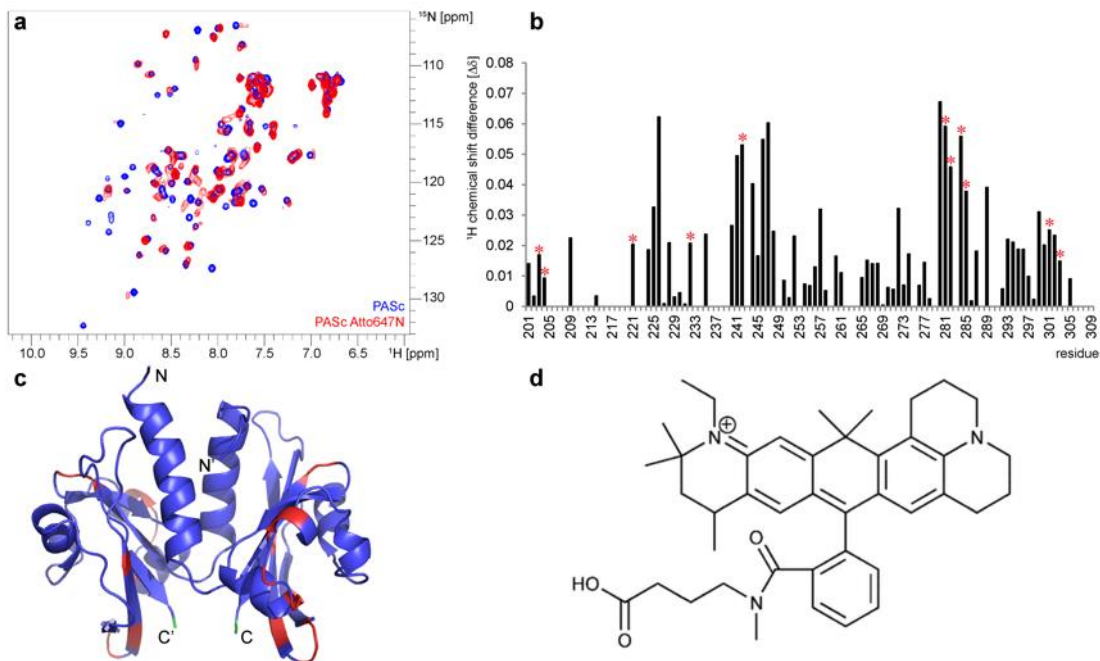**Supplementary Figure 5**

Crystal structure of GtPASc.

a, Crystal structure of GtPASc reveals a dimeric arrangement of monomers (green and grey) in which the N-terminal helices are swapped. **b,** The view from (a) is rotated by 90° for better visualization of N-terminal helix packing.

Supplementary Figure 6

Fourier shell correlation of two half data sets.

**a**, For the PASc domain dimer. The half-bit criterion yields a resolution of 1.9 Å. **b**, For the streptavidin complex. The half-bit criterion yields a resolution of 5.0 Å. The FSC was computed using Free FSC (IMAGIC).

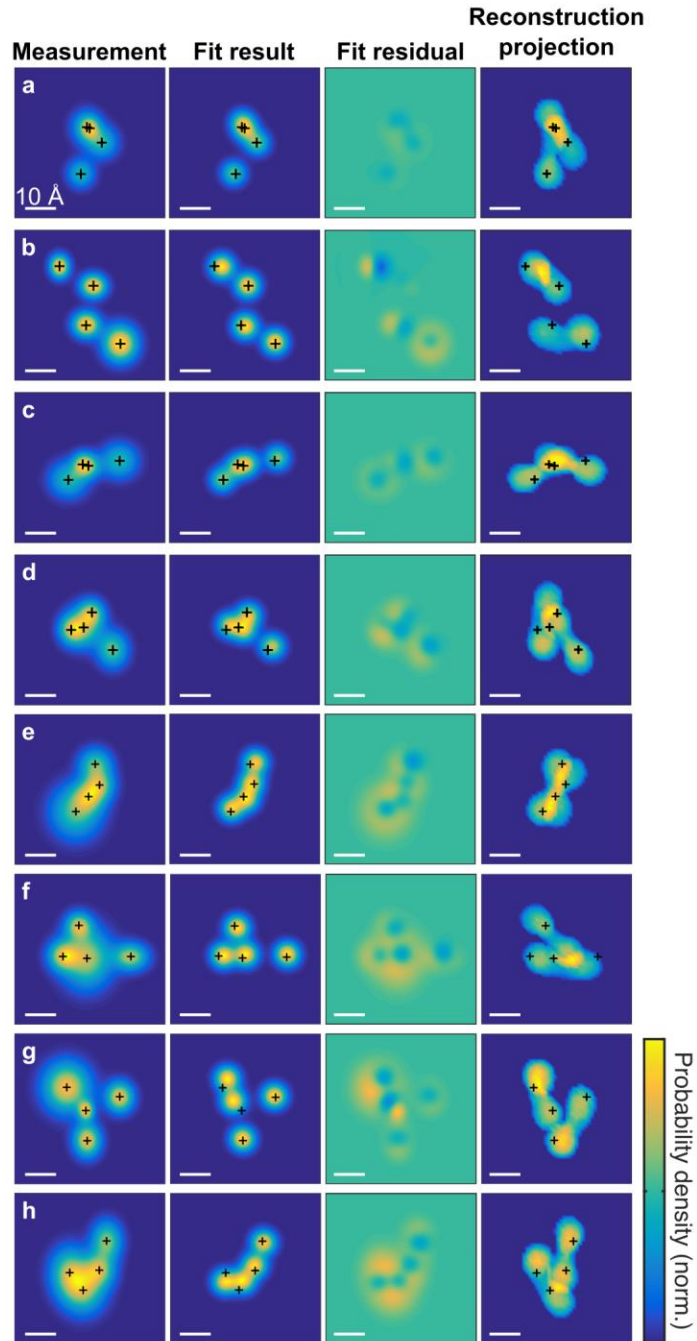**Supplementary Figure 7**

NMR on labeled PASc.

a, Overlay of ^{1}H,^{15}N-HSQC-spectra of 1 mM GtCitA PASc (blue) with 25 µM Atto647N-labeled PASc N308C (red). Peaks for unfolded PASc after dye labeling were not observable. Peaks corresponding to the β-scaffold are partially broadened out due to anisotropic effects from the dye molecules. **b,** Proton chemical shift difference of identified residues in Atto647N-labeled PASc compared to unlabeled PASc reference shifts. Only minor chemical shift changes are visible; an observed peak doubling for some residues (red asterisks) is likely caused by the achieved dye/protein ratio of 0.65, resulting in different molecular species in the NMR sample to be detected. **c,** Proton chemical shift differences of more than 0.03 ppm (red) mapped on the PASc crystal structure. Dye attachment site is shown in green. **d,** Chemical structure of the Atto647N dye molecule attached to the C-termini.
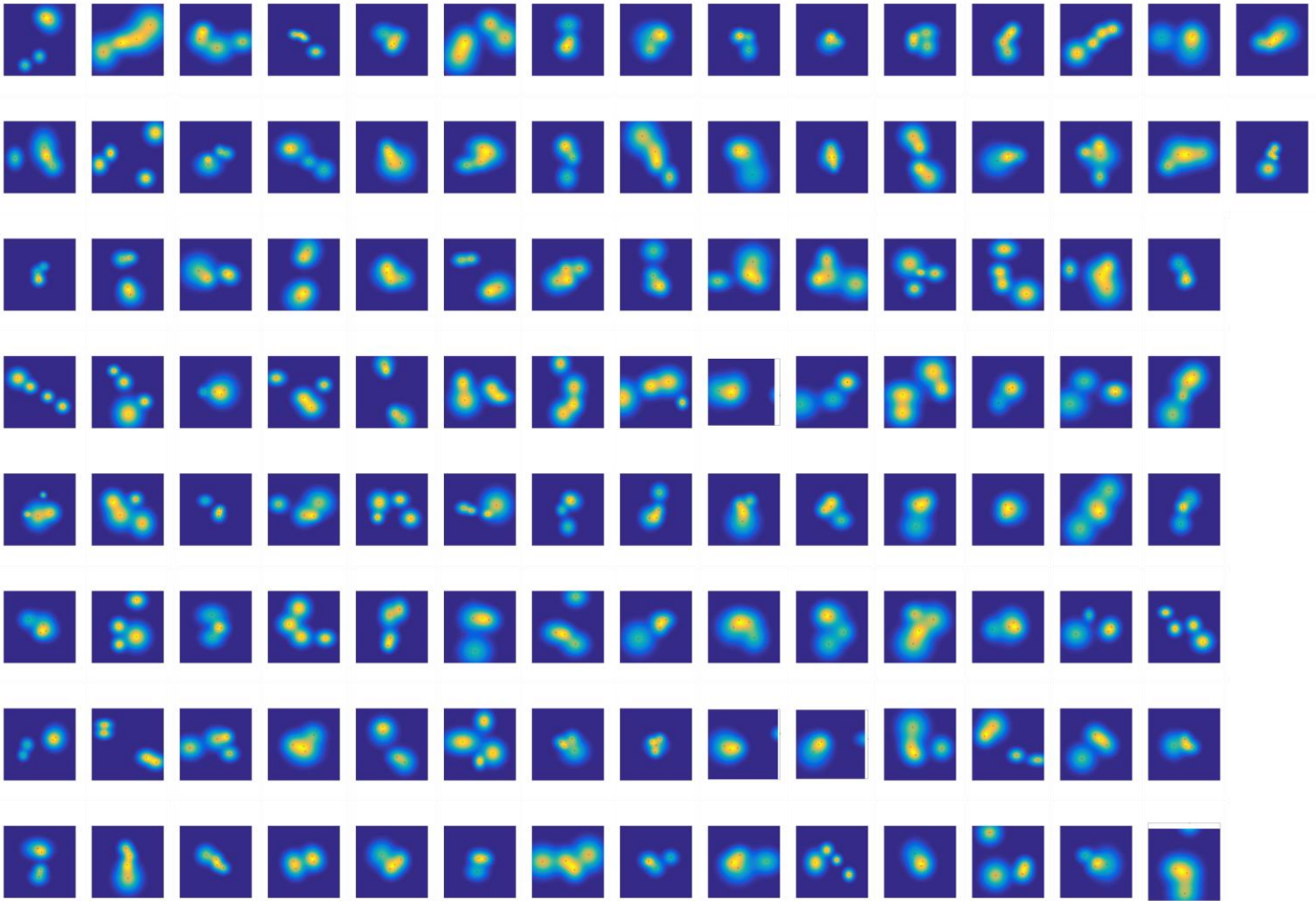
Supplementary Figure 8

**Complete data sets from the streptavidin measurements.**

Data for localization precisions better than 13 Å. Black crosses indicate the measured positions while the precision is encoded as the width of the 2D Gaussian probability distributions. Plots are 5 x 5 nm.

Supplementary Figure 9

**Protein orientation for streptavidin.**

Data sets form Fig. 3 (**a-d**) and additional data sets (**e–h**). Shown are the measurements, least squares fit results to the projection of a model volume, the fit residuals of the fit to the projection of a model volume, and least-squares fit results to projections of the reconstructed volume. See the Methods section for details.
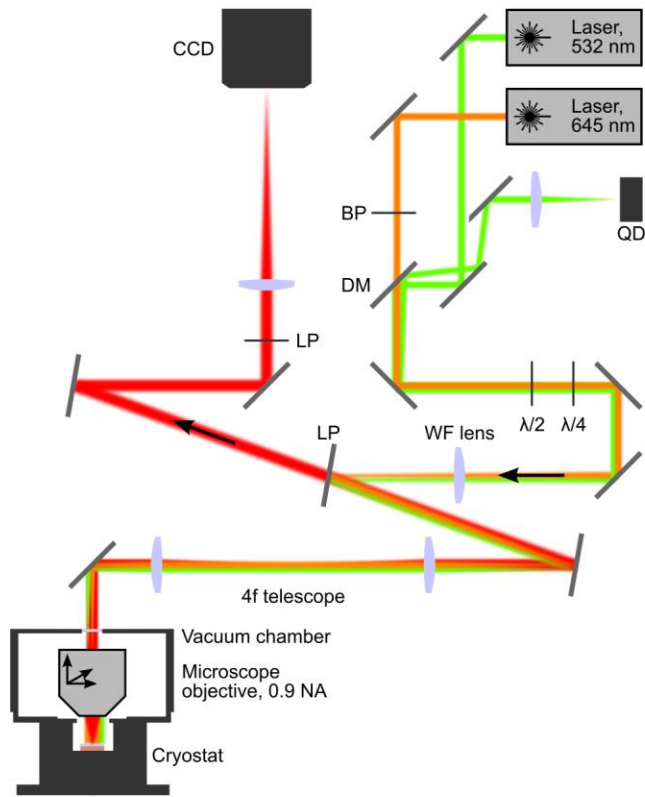
Supplementary Figure 10

Schematic of the cryogenic and optical setup.

Schematic of the beam path and optical components. BP - band pass filter; DM - dichroic mirror; QD - quad diode; λ/2 - half wave plate; λ/4 - quarter wave plate; WF lens - wide-field lens; LP - long pass filter; CCD - CCD camera. See the Methods section for a detailed description of the experimental setup.
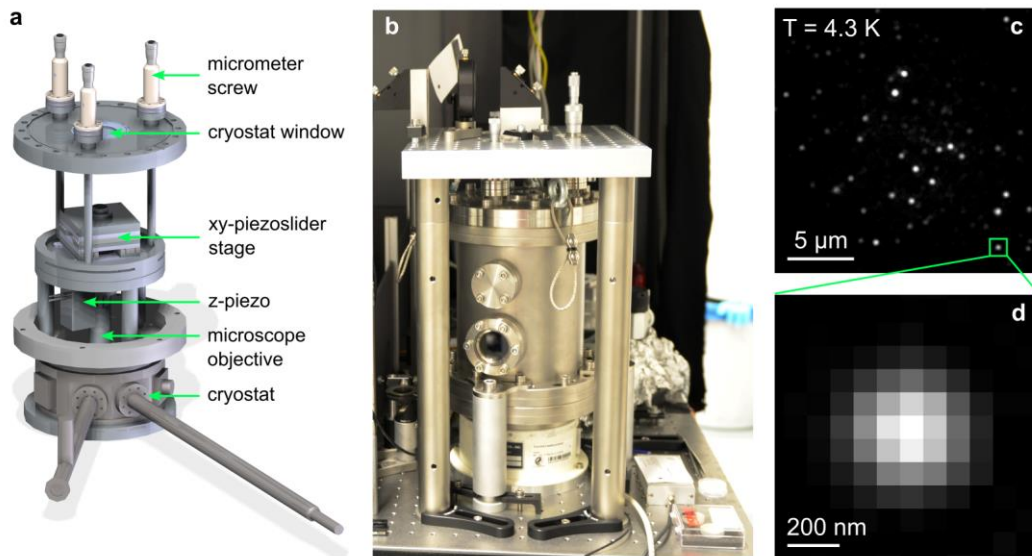
Supplementary Figure 11

Basics of COLD microscopy.

a, A commercial flow cryostat (lower part of the drawing) extended by a vacuum chamber (upper part; the walls are not shown for clarity) houses a microscope objective with a numerical aperture of 0.9. The sample is placed on a cold finger under the objective. See Methods for more details. **b**, Photograph of the cryostat with the vacuum chamber extension. **c**, Example of a wide-field fluorescence image recorded at T = 4.3 K with an integration time of 2 s. **d**, Zoom of one diffraction-limited spot.
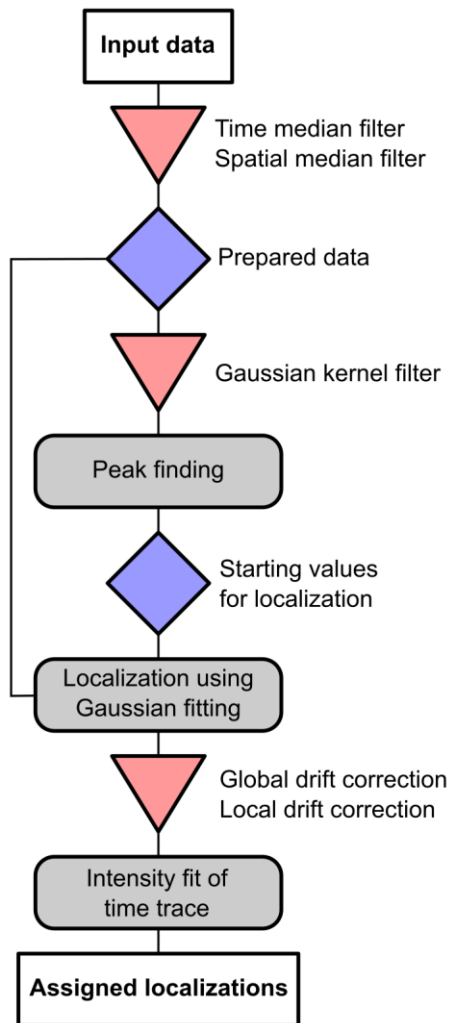
Supplementary Figure 12

Flow diagram describing the single-molecule data analysis.

See the Online Methods for a detailed description of the analysis.

(a)

n = 1.0

100 nm

dipole

z

θ

n = 1.5

n = 1.46

170 µm

(b)

bias < 0.025 nm

Inclination angle θ (degree)

Dipole distance z (nm)

Systematic localization error (nm)
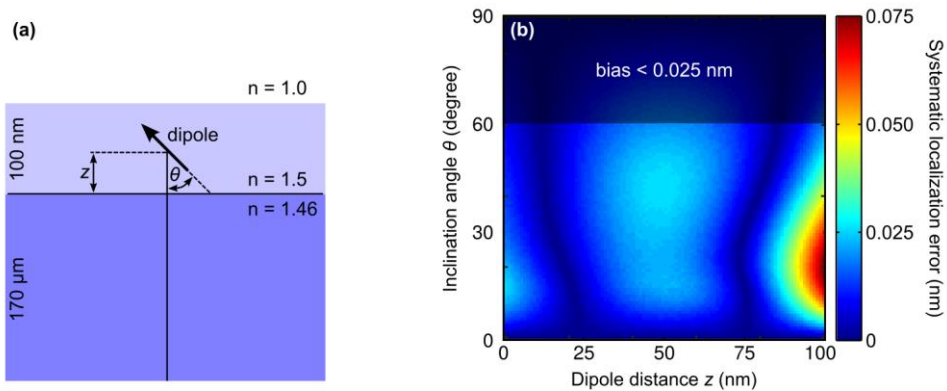
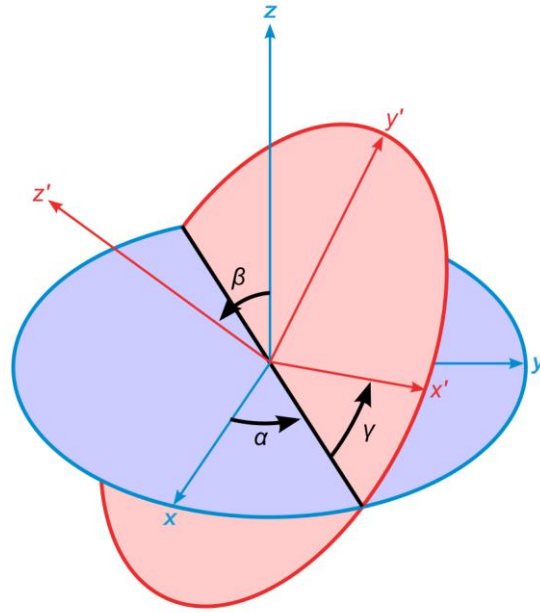**Supplementary Figure 13**

Systematic localization error.

a, Geometry for the simulations (see Supplementary Note 1). The molecules have a polar angle θ and a distance to the interface between the two media, z. Detection through the low-index medium. **b**, Simulation of the error in the localization accuracy as a function of z and θ, assuming NA = 0.9.
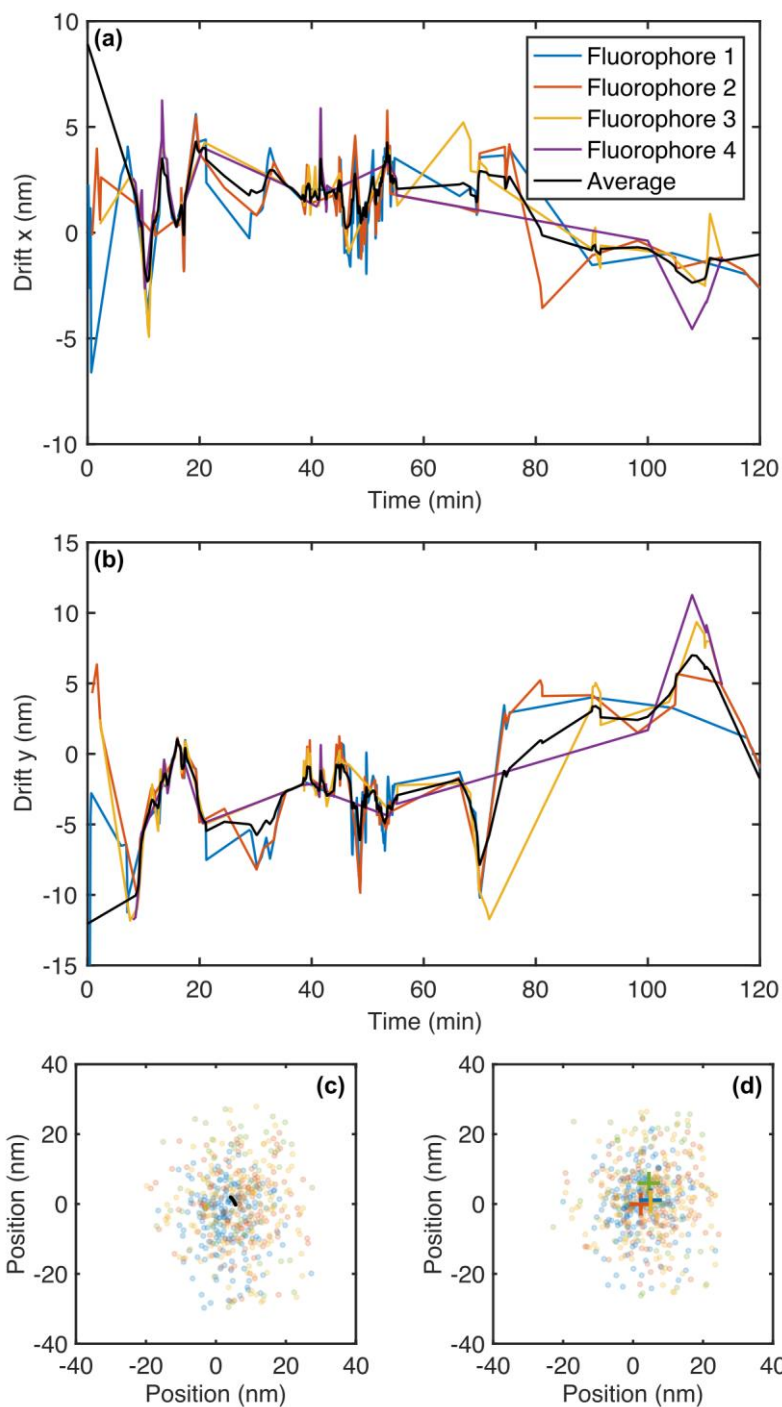
Supplementary Figure 14

Drift correction.

a,b, Example trace for the estimated localizations of the individual fluorophores (various colors). Weighted mean position for the molecule of interest in black. Estimated positions for all localizations from four fluorophores coupled to a molecule before (**c**) and after drift correction (**d**). Crosses mark the final positions of the four fluorophores. The sigma of the spread of individual localizations is on the order of 5-10 nm in accordance with our localization precision per frame, yielding the final localization precisions shown in Figs. 2c and 3c.

Supplementary Figure 15

Euler angle convention.

Rotations about the angles α, β and γ transform the coordinate system *xyz* into *x'y'z'*.

Supplementary Information

Cryogenic optical localization provides three-dimensional protein structure data with Angstrom resolution

Siegfried Weisenburger[1,2], Daniel Boening[1], Benjamin Schomburg[3], Karin Giller[3], Stefan Becker[3], Christian Griesinger[3] & Vahid Sandoghdar[1,2*]

[1] Max Planck Institute for the Science of Light, Erlangen, Germany.
[2] Department of Physics, Friedrich Alexander University (FAU) Erlangen-Nürnberg, Erlangen, Germany.
[3] Max Planck Institute for Biophysical Chemistry, Göttingen, Germany.

*: Correspondence should be addressed to V.S. (vahid.sandoghdar@mpl.mpg.de).

This Supplementary Information contains:

Supplementary Figure 12 Flow diagram describing the single-molecule data analysis.

Supplementary Figure 13 Systematic localization error

Supplementary Figure 14 Drift correction

Supplementary Figure 15 Euler angle convention

Supplementary Video 1 Increasing the quality of the 3D reconstruction with increasing the quality of the input data

Supplementary Video 2 Raw data recording

Supplementary Note 1 Localization accuracy

The localization accuracy quantifies how close the estimated position lies to the true position. One of the origins of systematic errors in determining the accuracy is the non-uniformity in the camera pixel response (PRNU) (1). In our experiments, the camera has a PRNU standard deviation of about 0.5 %. We verified by simulations that this causes a maximal systematic deviation from the true position of less than 0.5 nm. However, since both emitters are very close and feel the same PRNU landscape on the camera, this systematic error becomes negligible for our measurements.

Another effect that could influence the localization accuracy is the overlap of the PSFs of neighboring entities (proteins). This systematic error starts to be insignificant for inter-PSF distances of about nine pixels or more in our configuration. Thus, we avoided samples with too high of protein densities.

The strongest systematic localization error is typically due to the emission characteristics of a fixed dipole of arbitrary orientation at an interface. It is generally known that dipole emitters with an inclination angle outside the horizontal plane produce asymmetric PSFs. As a result, a localization method based on a centroid calculation or a 2D Gaussian fit cannot determine the actual position of the dipole emitter (2,3). Even in the case of rotating dipoles a systematic position error remains when the molecular rotation is partially impaired (4,5). It has been pointed out that this asymmetry and its associated localization error are much less pronounced if a microscope objective with low numerical aperture is used (3).

To investigate these effects for our case, we calculated artificial PSFs using the Kirchhoff vector approximation following the work of Mortensen and coworkers (6) and references therein. We verified that for our experimental setup the localization accuracy is not affected by the dipole orientation. The calculations were performed for an emission wavelength of 675 nm and our actual sample geometry where the emitter is placed inside a PVA layer with a refractive index $n = 1.5$ spin-coated on the fused cover slip with refractive index $n = 1.46$ (see Supplementary Fig. 13a). Supplementary Figure 13b shows the result for NA = 0.9, revealing that for increasing distance to the interface between the two media, z, the maximal systematic localization error increases and reaches about 0.075 nm at $z = 100$ nm. In the experiments reported in this work, we could only use a microscope objective with a low numerical aperture of NA = 0.9. As a result, dipole emitters with out-of-plane orientation were less efficiently excited, and large-angle components of the emission were not captured. Therefore, the localization accuracy of our measurements is not compromised in this arrangement.

Supplementary Table 1 | Overview of the recorded data and the experimental yield.

Data were filtered by all localization precisions better than 13 Å (streptavidin) and 6.5 Å (PASc domain dimer). We have performed a total of about 60 similar experiments over a period of seven months. The published data include 8372 single protein measurements.

	Streptavidin	PASc domain dimer
Identified proteins	6239	2133
After filtering	114	188
Yield	1.8 %	8.8 %

Supplementary Table 2 | GtCitA PASc crystallography.
X-ray data collection, phasing and refinement statistics of GtCitA PASc.

	Peak (PEAK)	Inflection (INFL)	High-energy remote (HREM)
Data collection statistics			
Wavelength (Å)	0.97929	0.97976	0.97163
X-ray source	X10SA, Swiss light source		
Detector	Pilatus 6M		
Space group	$P2_12_12_1$		
Unit cell parameters[a]	a=34.45 Å, b=74.03ß Å, c=75.08 Å, α=β=γ=90°	a=34.52 Å, b=74.28 Å, c=75.35 Å, α=β=γ=90°	a=34.51 Å, b=74.20 Å, c=75.26 Å, α=β=γ=90°
Resolution (Å)	1.78 (1.88-1.78)	1.99 (2.09-1.99)	1.97 (2.07-1.97)
No. of reflections (unique)	18,999	26,252	14,181
Completeness (%)	99.3 (96.5)	99.5 (96.7)	99.6 (97.6)
Mean I/(σI)	10.78 (2.4)	12.97 (2.65)	13.18 (3.82)
R_{int} (%)[b]	8.97 (50.64)	11.0 (51.46)	7.86(38.04)
Substructure solution (SHELX)			
$CC_{HREM/PEAK}$	31.8 % at 2.4 – 2.2 Å		
$CC_{HREM/INFL}$	32.3 % at 3.0 – 2.6 Å		
$CC_{PEAK/INFL}$	35.9 % at 3.5 – 3.0 Å		
No. of sites	4		
$CC_{ALL/WEAK}$	42.2/37.6		
Refinement statistics			
Final R-factor (%) Working set Working set + test set	18.50 18.65		
Final R_{free}[c]	21.65		
Twin fraction	0.095		
r.m.s.d. Bond lengths (Å) Bond angles (°)	0.019 2.14		
Mean B-value (Å^2) Monomer A Main chain atoms Side chain atoms Monomer B Main chain atoms Side chain atoms	26.58 32.45 26.99 33.03		
Solvent (%)	37		
No. of protein residues	221		
No. of glycerol molecules	4		
No. of phosphate molecules	3		
No. of water molecules	51		
Ramachandran plot (% of residues in) Most favoured regions Additionally allowed regions Disallowed regions	98.52 1.48 -		

[a] Values in parentheses are outer-resolution shells.
[b] $R_{int} = |F_0{}^2 - F_0{}^2(\text{mean})| / \Sigma(F_0{}^2)$.
[c] Five percent of reflections in thin shells were taken as the R_{free} set (7).

Supplementary Video 1 | Increasing the quality of the 3D reconstruction with increasing the quality of the input data.
Demonstration of the influence of the localization precision of the projection data on the 3D reconstruction. We gradually increase the requirement on the data quality by changing the filtering conditions from using only data sets with $20\ \text{Å} < \sigma_{Loc} < 30\ \text{Å}$ to using the best data sets with $\sigma_{Loc} < 13\ \text{Å}$ while keeping the number of input images similar. The movie shows an overlay of the reconstructed volumes (red) with the crystal structure. Isosurfaces are plotted at an isovalue of 0.68.

Supplementary Video 2 | Raw data recording.
Example of a wide-field fluorescence image stack recorded at T = 4.3 K with an integration time of 2 s. The movie shows the first hour raw data from a 2-hour recording. A black frame every 15 min indicates when automated refocusing is performed. Brightness has been adjusted for clarity.

Supporting Information references

1.   A. Pertsinidis, Y. Zhang & S. Chu Subnanometre single-molecule localization, registration and distance measurements. *Nature* **466**, 647 (2010).
2.   A. P. Bartko & R. M. Dickson Imaging Three-Dimensional Single Molecule Orientations. *J. Phys. Chem. B* **103**, 11,237 (1999).
3.   J. Enderlein, E. Toprak, & P. R. Selvin Polarization effect on position accuracy of fluorophore localization. *Opt. Express* **14**, 8111 (2006).
4.   J. Engelhardt *et al.* Molecular Orientation Affects Localization Accuracy in Superresolution Far-Field Fluorescence Microscopy. *Nano Lett.* **11**, 209 (2011).
5.   M. D. Lew, M. P. Backlund & W. E. Moerner Rotational Mobility of Single Molecules Affects Localization Accuracy in Super-Resolution Fluorescence Microscopy. *Nano Lett.* **13**, 3967 (2013).
6.   K. I. Mortensen *et al.* Optimized localization analysis for single-molecule tracking and super-resolution microscopy. *Nature Methods* **7**, 377 (2010).
7.   Brunger, A.T. Free R value: a novel statistical quantity for assessing the accuracy of crystal structures. *Nature* **355** (6359), 472-475 (1992).